

Tendon-Based Proprioception in an Anthropomorphic Underactuated Robotic Hand with Series Elastic Actuators

Jae-Hyun Lee, *Student Member, IEEE*, Jonghoo Park, *Student Member, IEEE*, and Kyu-Jin Cho, *Member, IEEE*

Abstract— Anthropomorphic underactuated hands are widely employed for their versatility and structural simplicity. In such systems, compact sensing integration and proper interpretation aligned with underactuation are crucial for realizing practical grasp functionalities. This study proposes an anthropomorphic underactuated hand that achieves comprehensive situational awareness of hand-object interaction, utilizing tendon-based proprioception provided by series elastic actuators (SEAs). We developed a compact SEA with high accuracy and reliability that can be seamlessly integrated into sensorless fingers. By coupling proprioceptive sensing with potential energy-based modeling, the system estimates key grasp-related variables, including contact timing, joint angles, relative object stiffness, and finger configuration changes indicating external disturbances. These estimated variables enable grasp posture reconstruction, safe handling of deformable objects, and blind grasping with proprioceptive-only recognition of objects with varying geometry and stiffness. Finger-level experiments and hand-level demonstrations confirmed the effectiveness of the proposed approach. The results demonstrate that tendon-based proprioception serves as a compact and robust sensing modality for practical manipulation without reliance on vision or tactile feedback.

I. INTRODUCTION

Anthropomorphic robotic hands have been widely adopted to replicate the functionality of the human hand. Among various actuation strategies, underactuated hands are extensively employed due to their structural simplicity, lightweight construction, and adaptability to diverse object geometries [1], [2]. As manipulation fundamentally involves interaction between the hand and the object, it is essential to sense grasp states throughout the interaction [3]. For instance, capturing finger configuration and force information remains essential for understanding object properties and interaction dynamics, thereby supporting the decision-making process during manipulation [4]. In underactuated hands, however, inherent uncertainty arising from interdependent joint motions complicates grasp state sensing [1], [5]. Accordingly, sensing approaches tailored to the distinctive features of underactuated mechanisms are required.

Human manipulation relies mainly on sensory feedback from vision, touch, and proprioception [6], [7], and these modalities have also been exploited in robotic hands. Vision

This work has been submitted to the IEEE for possible publication. Copyright may be transferred without notice, after which this version may no longer be accessible.

This work was supported by the National Research Foundation of Korea (NRF) Grant funded by the Korean Government (MSIT) (RS-2023-00208052).

All authors are with the BioRobotics Laboratory (BRL), Soft Robotics Research Center (SRRC), Department of Mechanical Engineering, Seoul National University (SNU), Seoul 08826, Korea (e-mail: lajaha37@snu.ac.kr; jpark608@snu.ac.kr; kjcho@snu.ac.kr).

provides global spatial information but limited force-related feedback and is highly sensitive to occlusion and lighting [8], [9]. To overcome these limitations of vision, robotic hands have primarily relied on touch, which provides direct contact information at the object interface [10]. However, integrating bulky tactile sensors into fingers undermines the inherent advantages of underactuated mechanisms, which lie in their compact and simple structure [11]. Moreover, since tactile sensors directly experience external forces through contact, they face challenges with durability and reliability [11], [12]. On the other hand, proprioception within the human sensorimotor system provides internal information about force and position [13]. Extending this concept to robotic hands enables sensing without external hardware, thereby facilitating simpler designs, easier assembly, and improved maintainability [14]. Furthermore, because proprioception is fundamentally decoupled from direct environmental interactions, it delivers robust performance that remains unaffected by contact conditions [15], [16].

In previous work, motor current has been used as a surrogate for proprioception, but its accuracy is constrained by electrical noise and transmission friction, which obscure reliable force estimation [17], [18]. Therefore, more direct approaches—such as load cells [15] or torque sensors [5], [19], fiber Bragg gratings (FBG) sensors [14], and series elastic actuators (SEAs) [16], [20], [21], [22], [23]—have been explored for measuring internal actuation force. However, applying them to anthropomorphic underactuated hands introduces two major challenges. First, achieving compact integration of proprioceptive sensing mechanisms while ensuring high sensing performance is challenging. Existing implementations often take the form of bulky grippers or hands with enlarged bases and palms, limiting their applicability in anthropomorphic hands [16], [19], [20], [21]. Second, previous studies lack a comprehensive interpretation and utilization of the implicit force signals of underactuation, which restricts practical grasp functionalities. Some works reported force profiles for object contact or stiffness, but the results were largely illustrative with little attention paid to the adaptive characteristics of underactuation [14], [21], [23]. Others relied solely on data-driven methods, which, due to a lack of physical interpretation, limit generalizability to broader scenarios [15], [19]. Another study modeled underactuated finger motion with stiffness to infer contact location, but its scope was constrained to localization under specific conditions without addressing other aspects of interaction, such as object deformation [5].

In this study, we present an anthropomorphic underactuated

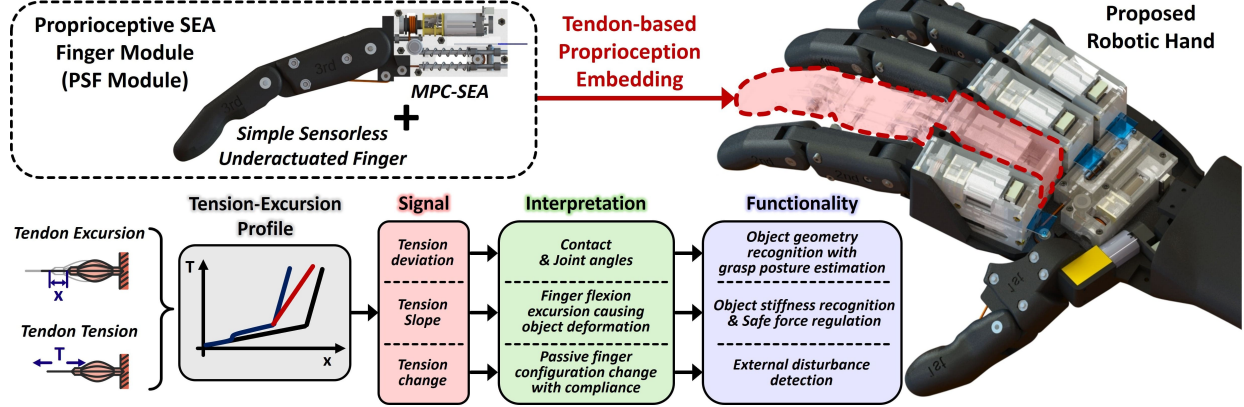


Fig. 1. Overview of the proposed anthropomorphic underactuated hand with tendon-based proprioception embedding through PSF modules.

hand that achieves comprehensive situational awareness of hand–object interaction and realizes practical grasp functionalities utilizing tendon-based proprioception. To this end, we designed a miniature proprioceptive cable-driven SEA (MPC-SEA) that can be seamlessly integrated within the hand, providing direct measurement of tendon tension with high accuracy and reliability. Its compactness is achieved through a simplified sensing and guiding scheme, while ensuring stable performance under repeated operation. When combined with simple underactuated fingers without any tactile sensors or joint encoders, the MPC-SEA forms a proprioceptive SEA finger (PSF) module that provides immediate sensing capability to sensorless hands, as shown in Fig. 1.

The PSF module acquires real-time tension and excursion measurements, which are combined with potential energy-based modeling of the underactuated finger to generate physically interpretable signals. These signals are further analyzed to infer grasp states of hand–object interactions, thereby enabling grasp functionalities. From a single tension–excursion profile, the hand can detect the timing of proximal and distal contacts, estimate each joint angle to reconstruct grasp posture, extract relative stiffness information, and identify external disturbances through SEA-driven compliance. All functions are executed in real time through a lightweight rule-based algorithm that combines computational simplicity with effective state estimation and stable grasp control. The proposed approach was validated through finger-level experiments—confirming finger modeling results and tension profile characterization—as well as extensive hand-level demonstrations, including grasp posture estimation of irregular objects, safe grasp force regulation for soft deformable objects without fracture, and blind grasping with proprioceptive-only recognition of objects varying in size, shape, and stiffness.

II. MPC-SEA

A. MPC-SEA Design

The physical appearance and specifications of the MPC-SEA are shown in Fig. 2(a). The module measures 48.8 mm \times 29.0 mm \times 17.6 mm and weighs 37.1 g, making it highly compact and lightweight. It can deliver up to 49 N of cable tension and pull the cable at a speed of 28.9 mm/s. The

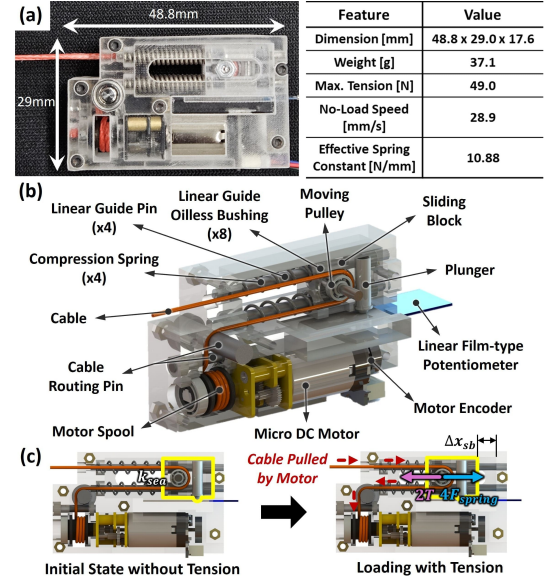


Fig. 2. Design of MPC-SEA. (a) Appearance and key specifications. (b) Structure and components. (c) Actuation mechanism.

structure of the MPC-SEA is shown in Fig. 2(b). Actuation is achieved by winding a cable (Dynext PU 0.9 mm, Amare Ropes, Italy) around a motor spool driven by a DC motor with a magnetic encoder (380:1 Micro Metal Gearmotor with 12 CPR Encoder, Pololu, USA). The cable is routed through a moving pulley housed in a sliding block, which translates linearly and compresses the spring when tension is applied, as shown in Fig. 2(c). Oilless bushings and pins guide linear motion, and the displacement of the sliding block is measured using a film-type potentiometer (ThinPot, Spectra Symbol, USA) via a spring-loaded plunger, ensuring consistent surface contact. The measured displacement is converted into cable tension using Hooke's law, with the effective spring constant determined by four parallel springs and the two-to-one pulley mechanism, as expressed in (1).

$$F_{\text{tension}} = \frac{F_{\text{spring}}}{2} = \frac{4k_{\text{sea}} \Delta x_{\text{sb}}}{2} = 2k_{\text{sea}} \Delta x_{\text{sb}} \quad (1)$$

where F_{tension} is the cable tension, F_{spring} is the restoring

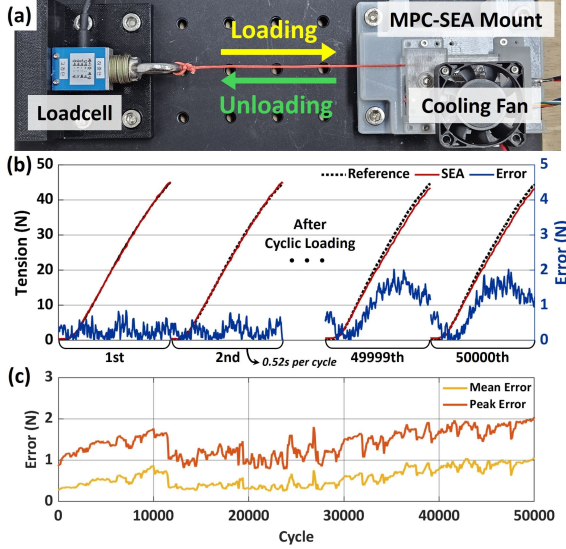


Fig. 3. Results of cyclic loading test of MPC-SEA. (a) Experiment setup. (b) Tension profiles over time for the first and last two cycles. (c) Mean error and peak error over cycles.

force of springs, k_{sea} is the spring constant of a single spring, and Δx_{sb} is the displacement of the sliding block.

The linear motion is implemented using oilless bushings and guide pins instead of a conventional ball screw, and displacement sensing relies on a film-type potentiometer with a plunger. This design selection achieves significant miniaturization compared to conventional linear SEAs, while maintaining high sensing accuracy and reliability. As a self-contained module, the MPC-SEA can be used immediately by simply connecting the cable to a finger.

B. MPC-SEA Experiment

To evaluate the accuracy and reliability of the MPC-SEA's tension sensing, a cyclic loading test was conducted. As shown in Fig. 3(a), the cable of a fixed MPC-SEA was connected to a load cell (333FDX, KTOYO, Korea). Each cycle consisted of loading from 0 N to 45 N ($\approx 90\%$ of maximum tension) and then unloading back to 0 N. The tension was recorded over loading, which is relevant to grasping, and compared with the reference tension measured by the load cell. A total of 50,000 cycles was performed.

Fig. 3(b) shows the tension profiles over time for the first and last two cycles. In the first two cycles, the error remained below 0.9 N across the entire range, indicating high accuracy. In the last two cycles, the error increased slightly in the higher-tension range, with a peak error of about 2 N. However, considering 50,000 cycles of severe repetitive loading, the sensing performance was well preserved. Errors mainly arose from transmission friction, spring nonlinearities, and misalignment between the sliding block and the potentiometer due to assembly tolerances. Fig. 3(c) shows the mean error and peak error, computed over all timesteps in each cycle. Although both error metrics increased compared to the initial cycles as the number of cycles approached 50,000, the mean error remained below 1 N and the peak error below 2 N throughout the entire test. These results confirm that the MPC-SEA maintained accurate

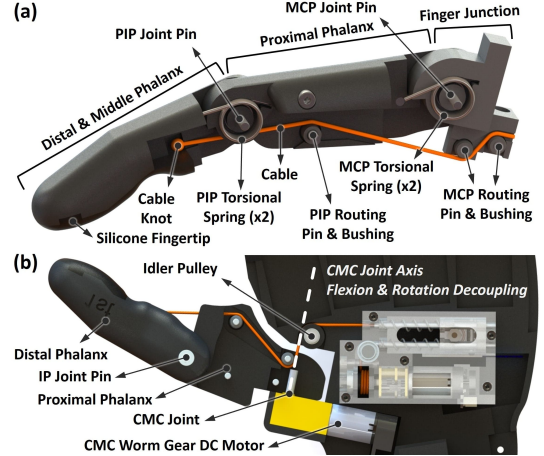


Fig. 4. Design of the finger and the thumb. (a) Finger (2nd–5th). (b) Thumb.

sensing performance even after 50,000 cycles, demonstrating the reliability of its structure and mechanism.

III. FINGER DESIGN, MODELING, AND EXPERIMENT

A. Finger and Thumb Design

All fingers (2nd–5th), except for the thumb (1st), share an identical design with only slight differences in dimensional parameters. The structure and components of the sensorless finger are shown in Fig. 4(a). Each finger consists of two joint degrees of freedom—metacarpophalangeal (MCP) and proximal interphalangeal (PIP) joints. Finger flexion is underactuated with tendon routing guided by oilless bushings, while extension is passively achieved via two torsional springs per joint. The fingertip surface is made of silicone (KE-1300T, Shin-Etsu Chemical, Japan) to increase friction.

Unlike the other fingers, the thumb features a single degree-of-freedom interphalangeal (IP) joint for flexion and an additional carpometacarpal (CMC) rotation joint for opposition, as shown in Fig. 4(b). The CMC rotation is actuated by a worm-gear DC motor (WG12F-1510E, Motorbank, Korea). Due to spatial constraints, the thumb cannot be directly connected to the MPC-SEA; instead, it is routed through an idler pulley. In this configuration, the tendon path passes through the CMC joint axis, thereby decoupling flexion from rotation.

B. Finger Modeling

To model the relationship between tendon excursion, tendon tension, and joint angles of the two underactuated joints, the minimum potential energy principle was applied, consistent with previous approaches in [12], [24]. Friction was neglected, and quasi-static movement was assumed. The system's total energy E_{Total} comprises the elastic energy E_e from the SEA spring and the extension torsional springs, along with gravitational energy E_g , as expressed in (2), (3), (4).

$$\begin{aligned}
 E_e(\theta_1, \theta_2, x) = & 4 \cdot 0.5 \cdot k_{\text{sea}} \cdot \left[\frac{x - \ell(\theta_1, \theta_2)}{2} \right]^2 \\
 & + 2 \cdot 0.5 \cdot k_1 \cdot (\theta_{\text{pre1}} + \theta_1)^2 \\
 & + 2 \cdot 0.5 \cdot k_2 \cdot (\theta_{\text{pre2}} + \theta_2)^2
 \end{aligned} \tag{2}$$

$$E_g(\theta_1, \theta_2) = m_1 \cdot g \cdot (\hat{\mathbf{z}}^\top R_{\text{hand}} R_j(\theta_{i1} + \theta_1) L_{c1}) + m_2 \cdot g \cdot [\hat{\mathbf{z}}^\top R_{\text{hand}} (R_j(\theta_{i1} + \theta_1) L_1 + R_j(\theta_{i1} + \theta_1 + \theta_{i2} + \theta_2) L_{c2})] \quad (3)$$

$$E_{\text{Total}}(\theta_1, \theta_2, x) = E_e(\theta_1, \theta_2, x) + E_g(\theta_1, \theta_2) \quad (4)$$

where the subscripts 1 and 2 denote the MCP and PIP joints, respectively; θ_1 and θ_2 are the joint angles with initial offset θ_{i1} and θ_{i2} ; x is the tendon excursion; $\ell(\theta_1, \theta_2)$ is the tendon length required to achieve the corresponding joint angles; k_{sea} is the SEA spring constant; k_1 and k_2 are the torsional spring constants with preloaded angles θ_{pre1} and θ_{pre2} ; m_1 and m_2 are the phalanx masses with center-of-mass position vectors L_{c1} and L_{c2} ; L_1 is the position vector from the MCP to the PIP joint; g is the gravitational acceleration; R_{hand} is the rotation matrix of the hand wrist; $R_j(\cdot)$ is the rotation matrix about the finger joint axis; and $\hat{\mathbf{z}}$ is the unit vector along the gravitational z -direction.

The optimization problem, formulated as shown in (5), aims to minimize the total energy of the system. The tendon excursion was discretized into small steps, and at each step, the state with the minimum energy was selected as the next step's state. Consequently, the only decision variables were the two joint angles, since the SEA spring displacement—and thus the tension—could be readily obtained by $\Delta x_{\text{sb}} = (x - \ell(\theta_1, \theta_2))/2$. The constraints were defined by the joint range of motion, expressed as RoM_j , and by the elastic limits of the SEA spring, expressed as $x_{\text{sb},\text{max}}$. This nonlinear optimization problem was solved in MATLAB using the sequential quadratic programming (SQP) algorithm. The modeling results are presented together with the experimental results in Section III-D.

$$\begin{aligned} \min_{\theta_1, \theta_2} \quad & E_{\text{Total}}(\theta_1, \theta_2) \\ \text{s.t.} \quad & 0 \leq \theta_{ij} + \theta_j \leq \text{RoM}_j, \quad j \in \{1, 2\}, \\ & 0 \leq \frac{x - \ell(\theta_1, \theta_2)}{2} \leq x_{\text{sb},\text{max}} \end{aligned} \quad (5)$$

C. Tension Profile Characterization

Fig. 5(a) illustrates the profiles of finger-object contact events for different grasp types. In an underactuated finger, the proximal and distal phalanges can sequentially contact the object, allowing the finger to adaptively wrap around it, or contact can occur only at the distal phalanx [25]. Contact is indicated by deviation from the free-flexion reference. Proximal contact constrains MCP motion, preventing the finger from following its original minimum-energy trajectory, which results in a slight upward shift of the tension profile. Distal contact halts finger motion, leaving only the SEA spring to compress and producing a sharp slope increase with an inflection point. The corresponding contact excursion can then be mapped to the angles of both joints with $\ell(\theta_1, \theta_2)$.

Fig. 5(b) presents tension profiles during the loading phase after distal contact, depending on the level of object deformation. For rigid objects, the slope theoretically matches the SEA spring constant, whereas for soft objects, the finger continues

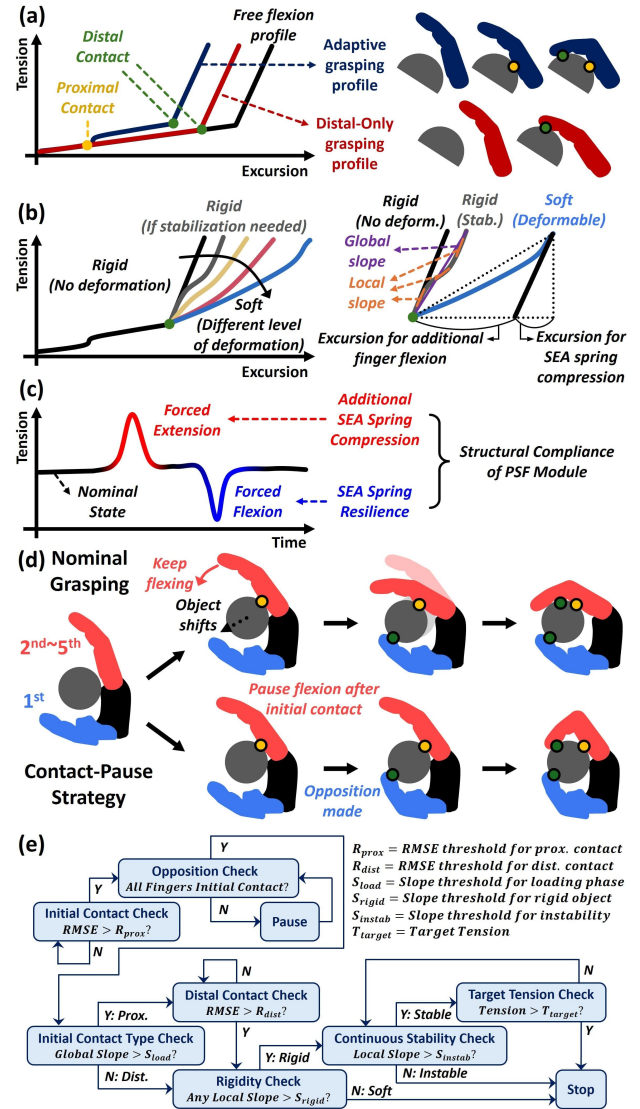


Fig. 5. Tension profile characterization and grasp algorithm. (a) Tension profiles reflecting contact events for different grasp types. (b) Tension profile reflecting object deformation and relative stiffness. (c) Tension profile reflecting finger configuration changes by external disturbances. (d) Contact-pause strategy to prevent object displacement and maintain the initial location. (e) Rule-based grasping algorithm.

to flex even after distal contact, yielding a reduced slope with object deformation. Thus, the slope indicates the portion of the tendon excursion contributing to object deformation and provides insight into object stiffness. Both local slope, which reflects instantaneous changes, and global slope, measured from the contact excursion, can be considered. Even for rigid objects, slight motion may occur until the object's configuration stabilizes due to inter-finger force equilibrium. Consequently, the global slope is suitable when evaluating the overall degree of deformation, while the local slope is more desirable for identifying intervals exhibiting rigid-like stiffness. Although the absolute value of object stiffness is not directly obtainable due to the indeterminate contact location, rigid and soft objects can be clearly distinguished, and relative stiffness comparisons remain valid within the same configuration.

Fig. 5(c) shows tension profiles under externally induced

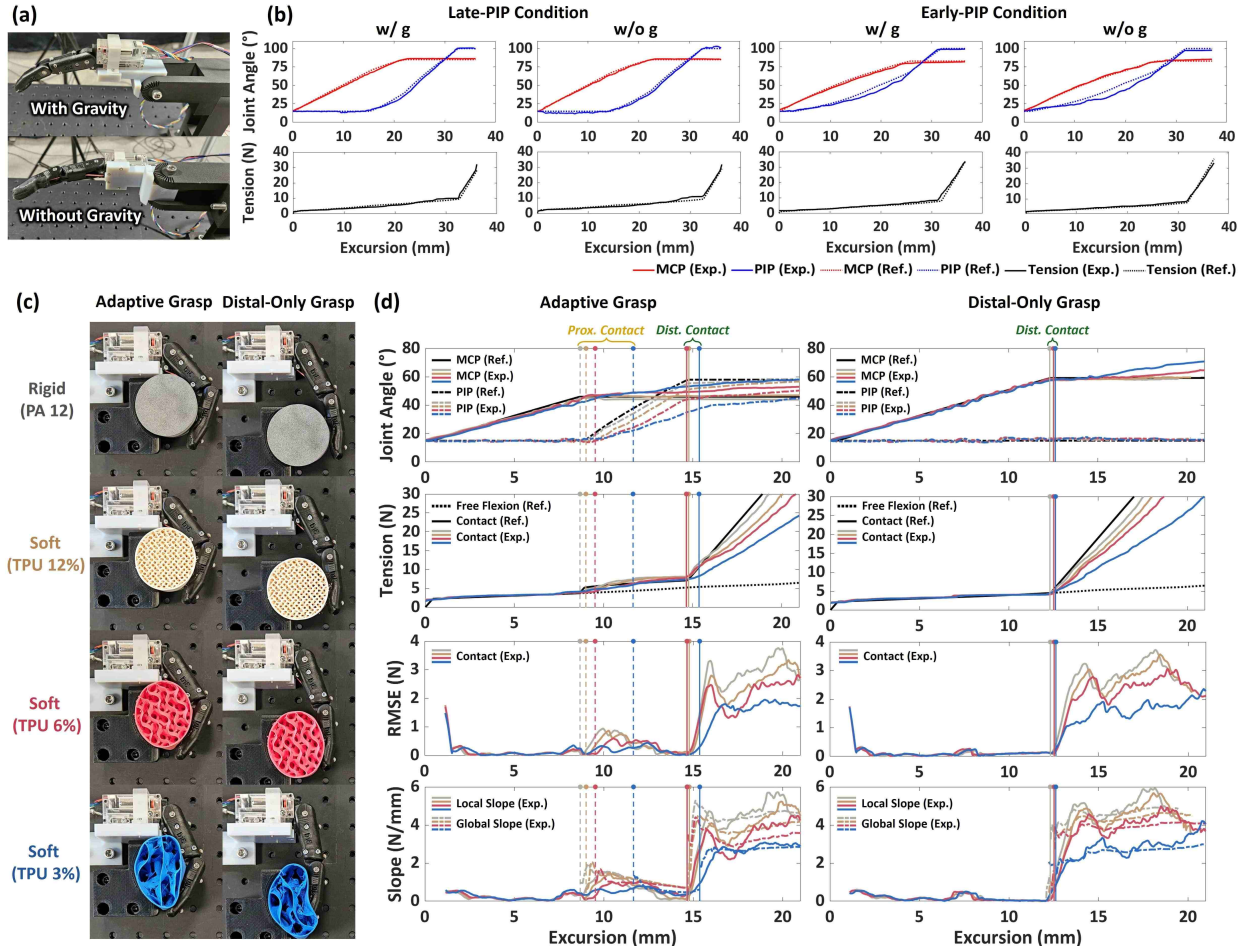


Fig. 6. Results of finger actuation experiments (a) Experimental setup for free-flexion cases. (b) Free-flexion results for joint angles and tension. (c) Experimental setup for finger-object contact cases. (d) Finger-object contact results for joint angles, tension, RMSE, and slope.

finger configuration changes when a finger is partially flexed or holding an object. Forcibly extending the finger compresses the SEA spring further and increases tension, while forcibly flexing the finger or losing support from the object being held releases the spring and reduces tension. These responses demonstrate that the PSF module can detect external disturbances through its structural compliance: flexion compliance is inherent to tendon-driven mechanisms, whereas extension compliance is uniquely enabled by the SEA.

When estimating joint angles from contact detection and relative stiffness from slope, it is critical to constrain the object, which is typically achieved through thumb opposition. If a finger contacts the object before opposition, object pushing may occur as in the nominal grasping case in Fig. 5(d), displacing the object and introducing errors in estimation. To prevent this, a strategy similar to that of [26] was adopted: the first contacting finger is paused, and actuation resumes only after all fingers have made contact. This contact-pause strategy ensures that the object retains its initial position.

Contact detection from tension profile deviations is implemented using a sliding-window root-mean-square error (RMSE) method. The control loop operates at 1000 Hz, and RMSE is computed over a 50-sample window (50 ms). Before computation, the window is offset-corrected by aligning its

first sample to the corresponding reference value, ensuring consistent comparison with the reference profile. When the RMSE exceeds a predefined threshold R_{prox} , contact is detected and assigned to the midpoint of the window. To identify the initial contact type, the global slope is evaluated 75 ms after threshold crossing: values below S_{load} indicate proximal contact, while values above S_{load} indicate distal contact. If the initial contact is distal, the system proceeds directly to rigidity evaluation; if proximal, an additional RMSE-based search with threshold R_{dist} is conducted to detect distal contact before rigidity evaluation. The object is classified as rigid if any local slope, computed over a sliding window, exceeds S_{rigid} ; otherwise, it is deemed soft, and actuation is halted to regulate the grasping force, thereby preventing excessive deformation or fracture. To prevent misclassification or instability due to object stabilization, actuation is also terminated if the local slope falls below S_{instab} during loading. This rule-based strategy enables accurate estimation and stable grasp execution. Fig. 5(e) illustrates the entire grasping algorithm implemented for each finger.

D. Finger Actuation Experiment

To validate the accuracy of the modeling and the plausibility of the tension profile characterization, experiments

were conducted using a PSF module. Fig. 6(a) shows the setup for the free-flexion cases. Two representative orientations were selected: one with the palm facing sideways, unaffected by gravity, and another with the palm facing downward, subject to gravity. The torsional spring preloads of the MCP and PIP joints were also adjusted in two combinations to examine different actuation sequences: a late-PIP condition (MCP 36°/PIP 32°) and an early-PIP condition (MCP 28°/PIP 12°). The results are shown in Fig. 6(b). Under the late-PIP condition, the joint angles and tension matched the modeling reference with high accuracy. Under the early-PIP condition, slight discrepancies were observed in the PIP joint, likely because the weaker preload caused two joints to actuate more simultaneously, making the motion susceptible to friction. In both conditions, gravitational effects were minimal, as the finger was lightweight with relatively high joint stiffness, making spring forces dominant. To prevent the ejection in underactuated fingers and to secure a larger workspace, the late-PIP condition was selected as the final parameter.

Fig. 6(c) shows the setup for finger-object contact cases. Both adaptive and distal-only grasp types were considered with a fixture substituting for the role of thumb opposition. The test object was a 50 mm diameter cylinder; the rigid one was 3D-printed in PA12 (3D HR PA12, HP Inc., USA), and the soft ones were printed in TPU (VarioShore TPU, colorFabb, Netherlands) with varying infill densities. A gyroid infill pattern, which is nearly isotropic [27], was selected. For this experiment, actuation was not halted as in Fig. 5(e) but instead uniformly increased to 40 N to observe slope variations by deformation during loading. The RMSE thresholds for contact detection were set to $R_{\text{prox}} = 0.4$ N and $R_{\text{dist}} = 1.0$ N, with the loading slope threshold set to $S_{\text{load}} = 2$ N/mm.

Fig. 6(d) presents the modeled reference and experimental joint angles and tension profiles with RMSE and slopes. The reference profiles for joint angles and tension were generated for the case of a rigid object. In both grasp types, the profiles clearly exhibited the distinct proximal and distal contact patterns characterized in Fig. 5(a), and the slopes varied noticeably with stiffness level as in Fig. 5(b). In both grasp types, the slope for the rigid object was slightly lower than the reference, likely due to deformation of the silicone fingertip. Since this deformation consistently occurs at every contact, the experimentally measured rigid slope can serve as a practical reference. Between the two slope metrics, the local and global slopes exhibited similar tendencies, but the global slope proved more stable and reliable for distinguishing relative stiffness levels. In the adaptive grasp, rigid objects caused the MCP angle to remain fixed after proximal contact, whereas soft objects allowed the MCP angle to continue increasing slightly along with the PIP joint. This difference makes estimation more challenging for soft objects. Nevertheless, the rule-based contact detection scheme naturally accounts for such interaction. Since the weak resistance of soft objects produces only a small deviation from the reference profile, it delays the threshold crossing. These results yielded larger estimated MCP angles and smaller PIP angles, thereby mitigating potential errors and preserving consistency with the actual grasp dynam-

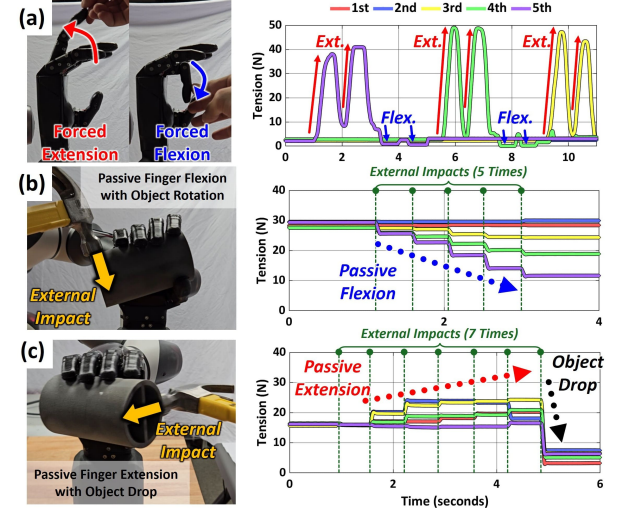


Fig. 7. Disturbance detection with SEA-driven compliance. (a) Tension change during forced flexion and extension of an initially flexed finger. (b), (c) Passive finger flexion and extension caused by external impacts.

ics. Meanwhile, in the distal-only grasp—where the interaction is simpler than in the adaptive case—the contact timing was consistent regardless of object stiffness.

IV. GRASP FUNCTIONALITY IMPLEMENTATION

A. Disturbance Detection with Compliance

Building on the characterization in Fig. 5(c), disturbance detection through structural compliance was experimentally verified. As shown in Fig. 7(a), when a finger preloaded to about 2.5 N was forcibly extended, the SEA spring compressed further with increased tension, whereas forced flexion caused the spring to release with decreased tension. Fig. 7(b) and (c) show responses to hammer strikes on a grasped cylinder: in (b), ulnar-side rotation of the object induced additional flexion of the 3rd–5th fingers, whereas in (c), repeated impacts gradually extended the fingers until the object was released, accompanied by a sharp tension drop. These results demonstrate that the system can detect the nature of external disturbances through tension changes, while compliance simultaneously enables the fingers to maintain contact without damage, even under external impacts such as hammer strikes that alter the object’s configuration.

B. Grasp Posture Estimation

The joint angle estimation of individual fingers was extended to reconstruct the overall grasp posture. Three irregularly shaped YCB objects [28] were selected: a power drill, a wine glass, and a plastic pear. The drill and glass correspond to adaptive grasps, while the pear corresponds to a distal-only grasp. Actual joint angles were measured with a motion capture system (OptiTrack, NaturalPoint Inc., USA). Two reflective markers were attached to each phalanx, and joint angles were computed from changes in marker vectors between initial and final configurations. As shown in Fig. 8, the estimated posture from tension profiles was visualized on a CAD model and compared with the actual posture. The

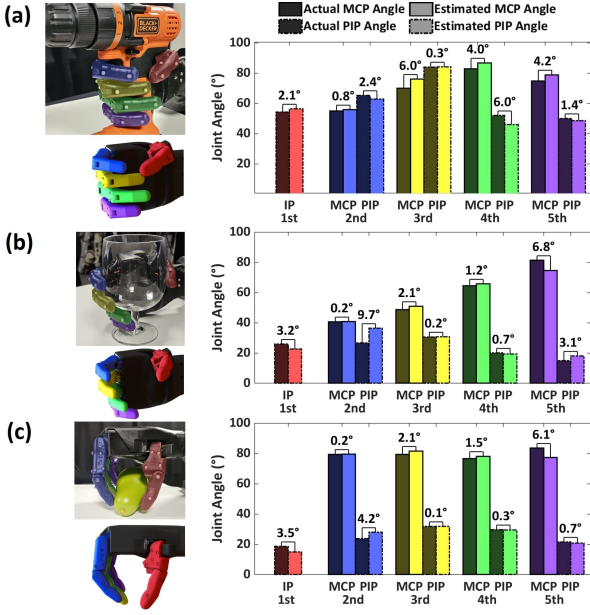


Fig. 8. Comparison of the actual and estimated grasp posture for different objects from YCB object set. (a) Hand drill. (b) Wine glass. (c) Plastic pear.

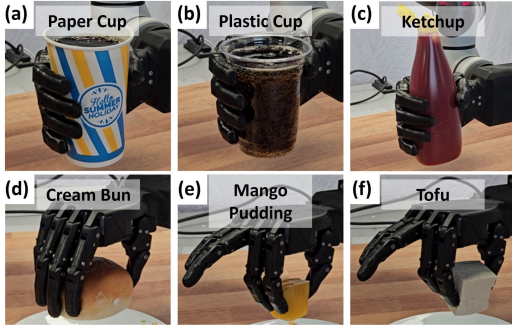


Fig. 9. Safe grasp force regulation for deformable objects. (a) Paper cup. (b) Plastic cup. (c) Ketchup. (d) Cream bun. (e) Mango pudding. (f) Tofu.

average error per joint angle was 3.0° for the drill and glass and 2.1° for the pear, indicating high overall accuracy.

C. Safe Grasp Force Regulation for Deformable Objects

With rigidity evaluation in the grasping algorithm, deformable object grasping was demonstrated on common objects, including a paper cup, plastic cup, ketchup, cream bun, mango pudding, and tofu, as shown in Fig. 9. The first four objects were grasped with all five fingers, while the last two smaller ones were grasped using a tripod pinch. In all cases, finger flexion was halted appropriately after distal contact, preventing excessive deformation or fracture while enabling stable lifting.

D. Blind Grasping with Object Recognition

A blind grasping task with object recognition was conducted to demonstrate the integrated proprioceptive functionality. This task was inspired by the way humans sweep their hands across a table to locate and grasp objects without vision. As shown in Fig. 10(b), the hand mounted on a robot manipulator (RB5-850, Rainbow Robotics, Korea) explored a defined search area

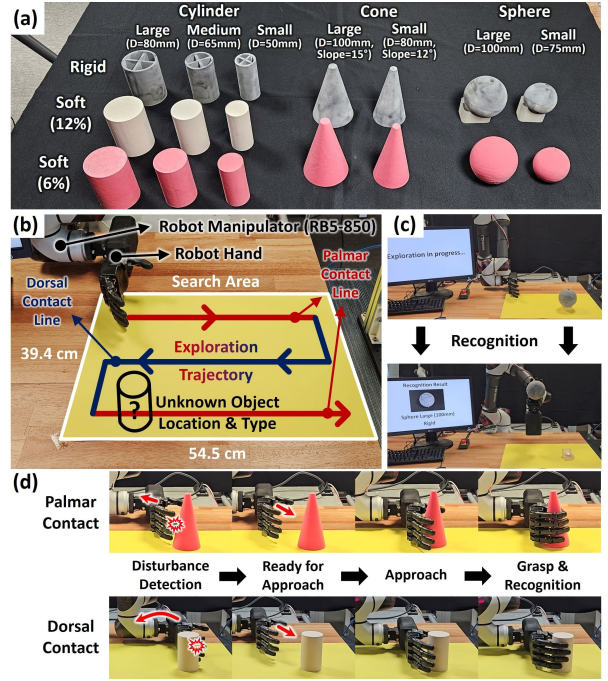


Fig. 10. Blind grasping and object recognition demonstration. (a) Sample Objects with varying size, shape, and stiffness. (b) Task setup with exploration trajectory. (c) Task completion with object recognition result. (d) Execution of approach after palmar and dorsal contact.

by executing three consecutive sweeps—palmar, dorsal, and palmar. Before exploration, the fingers were flexed slightly for 50 ms to preload tension, thereby enabling bidirectional disturbance detection. Once contact was detected, the hand executed a predefined approach and completed the grasp, with dorsal contacts leading to an approach from behind the object as shown in Fig. 10(d).

Seventeen objects with varying size, shape, and stiffness were used, including cylinders, cones, and spheres in rigid and soft forms, as shown in Fig. 10(a). All objects were fabricated with the same material as in Fig. 6(c). To prevent rolling or slipping during exploration, spheres were mounted on support bases, and soft objects had sandpaper attached to their bottoms. For classification, a simple k-nearest neighbors (k-NN) model ($k = 3$, Euclidean distance) was employed as a proof-of-concept demonstration. Object geometry (size and shape) was recognized using a kinematics-based approach [9], [29], while stiffness recognition was subsequently performed within each geometry category by comparing the average global slope across five fingers. The feature vector of the training dataset consisted of nine joint angles and the averaged global slope, collected from ten grasp trials per object. To enhance robustness against variability in the approach motion, the object positions were slightly varied during training. As depicted in Fig. 10(c), the system successfully identified unknown objects and displayed the recognition result, with the complete process provided in the supplementary video.

V. DISCUSSION & CONCLUSION

This study presented an integrated system for tendon-based proprioception in an anthropomorphic underactuated hand,

addressing hardware design for compact actuation as well as the analysis and application of proprioceptive tension profiles. To this aim, the MPC-SEA was developed as a compact module providing reliable tension sensing and enabling seamless embedding of proprioception within the hand. With an energy-based model, the tension profile serves as an informative grasp-state indicator, enabling comprehensive hand-object interactions throughout the entire grasp process. During reaching, contact detection enables joint angle estimation; during loading, tendon excursion associated with deformation supports relative stiffness evaluation; during holding, finger configuration changes reflected in tension indicate external disturbances. Additionally, these interaction variables offer consistent and quantitative grasp-state information, supporting applicability across different tasks and hardware settings. Experiments validated the sensing performance of the MPC-SEA and confirmed the characterization of tension profiles for hand-object interaction. In addition, demonstrations highlighted key functionalities including grasp posture estimation, safe handling of deformable objects, and proprioceptive recognition in blind grasping.

Despite these results, several limitations remain. First, the modeling neglects friction. While its effect was minimized in our system by using bearings and bushings, hardware with higher friction may experience larger estimation errors. Second, the approach depends on appropriate design parameters; for instance, overly weak torsional springs at the joints may lead to tension variations too small for reliable proximal contact detection. Finally, the interpretation of tension-excitation profiles is currently implemented through a rule-based algorithm, limiting robustness under unexpected or extreme grasping conditions. Future work will explore learning-based methods to process tension profile data, which may enable more generalized controllers capable of handling a wider range of situations.

REFERENCES

- [1] L. Birglen, T. Laliberté, and C. M. Gosselin, *Underactuated robotic hands*. Springer, 2007, vol. 40.
- [2] C. Piazza, G. Grioli, M. Catalano, and A. Bicchi, “A Century of Robotic Hands,” *Annual Review of Control, Robotics, and Autonomous Systems*, vol. 2, no. 1, pp. 1–32, May 2019.
- [3] H. Fan, T. Zhuo, X. Yu, Y. Yang, and M. Kankanhalli, “Understanding Atomic Hand-Object Interaction With Human Intention,” *IEEE Transactions on Circuits and Systems for Video Technology*, vol. 32, no. 1, pp. 275–285, Jan. 2022.
- [4] B. S. Homberg, R. K. Katzschmann, M. R. Dogar, and D. Rus, “Robust proprioceptive grasping with a soft robot hand,” *Autonomous Robots*, vol. 43, no. 3, pp. 681–696, Mar. 2019.
- [5] B. Belzile and L. Birglen, “Stiffness Analysis of Underactuated Fingers and Its Application to Proprioceptive Tactile Sensing,” *IEEE/ASME Transactions on Mechatronics*, vol. 21, no. 6, pp. 2672–2681, Feb. 2016.
- [6] R. S. Johansson and K. J. Cole, “Sensory-motor coordination during grasping and manipulative actions,” *Current opinion in neurobiology*, vol. 2, no. 6, pp. 815–823, 1992.
- [7] J. R. Flanagan, M. C. Bowman, and R. S. Johansson, “Control strategies in object manipulation tasks,” *Current Opinion in Neurobiology*, vol. 16, no. 6, pp. 650–659, Dec. 2006.
- [8] R. Calandra, A. Owens, D. Jayaraman, J. Lin, W. Yuan, J. Malik, E. H. Adelson, and S. Levine, “More Than a Feeling: Learning to Grasp and Regrasp Using Vision and Touch,” *IEEE Robotics and Automation Letters*, vol. 3, no. 4, pp. 3300–3307, Oct. 2018.
- [9] A. Boruah, N. M. Kakoti, T. Ali, and M. B. Malarvili, “Shape oriented object recognition on grasp using features from enclosure based exploratory procedure,” *International Journal of Intelligent Robotics and Applications*, vol. 7, no. 1, pp. 48–64, Mar. 2023.
- [10] S. Luo, J. Bimbo, R. Dahiya, and H. Liu, “Robotic tactile perception of object properties: A review,” *Mechatronics*, vol. 48, pp. 54–67, Dec. 2017.
- [11] S.-H. Kim, U. Jeong, and K.-J. Cho, “Multiparameter Remote Contact Force Sensor With Embedded Bend Sensing for Tendon-Driven Hand Robots,” *IEEE/ASME Transactions on Mechatronics*, vol. 29, no. 1, pp. 557–566, Feb. 2024.
- [12] X. Zhang, T. Zhu, I. Yamayoshi, and D. Hong, “Dexterity, Sensitivity and Versatility: An Under Actuated Robotic Hand with Mechanical Intelligence and Proprioceptive Actuation,” *International Journal of Humanoid Robotics*, vol. 17, no. 02, p. 2050006, Apr. 2020.
- [13] J. C. Tuthill and E. Azim, “Proprioception,” *Current Biology*, vol. 28, no. 5, pp. R194–R203, Mar. 2018.
- [14] J. Yi, B. Kim, K.-J. Cho, and Y.-L. Park, “Underactuated Robotic Gripper With Fiber-Optic Force Sensing Tendons,” *IEEE Robotics and Automation Letters*, vol. 8, no. 11, pp. 7607–7614, Jan. 2023.
- [15] Y. Yan, C. Cheng, M. Guan, J. Zhang, and Y. Wang, “Texture Identification and Object Recognition Using a Soft Robotic Hand Innervated Bio-Inspired Proprioception,” *Machines*, vol. 10, no. 3, p. 173, Mar. 2022.
- [16] Y. Yan, S. Guo, C. Lyu, D. Zhao, and Z. Lin, “SEA-Based Humanoid Finger-Functional Parallel Gripper With Two Actuators: PG2 Gripper,” *IEEE Transactions on Instrumentation and Measurement*, vol. 72, pp. 1–13, 2023.
- [17] H. Hu, Z. Xie, Y. Liu, C. Guo, B. Ma, Y. Liu, and H. Liu, “Force Sensing Strategy for the Antagonistic Variable Stiffness Hand,” *IEEE Sensors Journal*, vol. 24, no. 21, pp. 34 100–34 106, Jan. 2024.
- [18] P.-C. Yeh, Y.-S. Tsai, and C.-C. Lan, “A Compliant Gripper With Two-Dimensional Force Sensing on Each Finger,” *IEEE/ASME Transactions on Mechatronics*, vol. 29, no. 2, pp. 1041–1051, Apr. 2024.
- [19] J. Arolovitch, O. Azulay, and A. Sintov, “Kinesthetic-based In-Hand Object Recognition with an Underactuated Robotic Hand,” in *2024 IEEE International Conference on Robotics and Automation (ICRA)*, May 2024, pp. 18 179–18 185.
- [20] O. Kaya, G. B. Tağlıoğlu, and Ş. Ertuğrul, “The Series Elastic Gripper Design, Object Detection, and Recognition by Touch,” *Journal of Mechanisms and Robotics*, vol. 14, no. 1, p. 014501, Feb. 2022.
- [21] H. Hua, Z. Liao, and J. Zhao, “Design, Analysis, and Experiment of an Underactuated Robotic Gripper Actuated by Linear Series Elastic Actuator,” *Journal of Mechanisms and Robotics*, vol. 15, no. 2, p. 021002, Apr. 2023.
- [22] T. Chen and M. Ciocarlie, “Proprioception-Based Grasping for Unknown Objects Using a Series-Elastic-Actuated Gripper,” in *2018 IEEE/RSJ International Conference on Intelligent Robots and Systems (IROS)*, Oct. 2018, pp. 6675–6681.
- [23] X. Wu, H. Hua, C. Zhao, N. Shi, and Z. Wu, “A Back-Drivable Rotational Force Actuator for Adaptive Grasping,” *Actuators*, vol. 12, no. 7, p. 267, Jun. 2023.
- [24] L. U. Odhner, L. P. Jentoft, M. R. Claffee, N. Corson, Y. Tenzer, R. R. Ma, M. Buehler, R. Kohout, R. D. Howe, and A. M. Dollar, “A compliant, underactuated hand for robust manipulation,” *The International Journal of Robotics Research*, vol. 33, no. 5, pp. 736–752, Apr. 2014.
- [25] A. J. Spiers, M. V. Liarokapis, B. Calli, and A. M. Dollar, “Single-Grasp Object Classification and Feature Extraction with Simple Robot Hands and Tactile Sensors,” *IEEE Transactions on Haptics*, vol. 9, no. 2, pp. 207–220, Apr. 2016.
- [26] L. P. Jentoft, Q. Wan, and R. D. Howe, “Limits to compliance and the role of tactile sensing in grasping,” in *2014 IEEE International Conference on Robotics and Automation (ICRA)*, May 2014, pp. 6394–6399.
- [27] P. Bean, R. A. Lopez-Anido, and S. Vel, “Numerical Modeling and Experimental Investigation of Effective Elastic Properties of the 3D Printed Gyroid Infill,” *Applied Sciences*, vol. 12, no. 4, p. 2180, Jan. 2022.
- [28] B. Calli, A. Singh, A. Walsman, S. Srinivasa, P. Abbeel, and A. M. Dollar, “The YCB object and Model set: Towards common benchmarks for manipulation research,” in *2015 International Conference on Advanced Robotics (ICAR)*, Jul. 2015, pp. 510–517.
- [29] A. Vásquez and V. Perdereau, “Proprioceptive shape signatures for object manipulation and recognition purposes in a robotic hand,” *Robotics and Autonomous Systems*, vol. 98, pp. 135–146, Dec. 2017.